



Electrochemical impedance preprocessing with distribution of relaxation time transform

Bowen Yang, Dafang Wang*, Shiqin Chen, Xu Sun, Beike Yu

School of Mechatronics Engineering, Harbin Institute of Technology, Harbin, 150001, China



HIGHLIGHTS

- The DRT kernel inherently satisfies the K-K relations, leading to new EIS validation approach alternative to K-K.
- The impact of inductance on EIS is removed using DRT transform by correcting the high-frequency distortion.
- DRT-based manipulation of EIS data is introduced for the removal, modification and isolation of electrochemical processes.
- A scheme diagnosing the nonlinearity and time-variance for low-frequency EIS is presented.

ARTICLE INFO

Keywords:

Electrochemical impedance spectroscopy
Distribution of relaxation time
Lithium-ion battery
High-frequency distortion correction
Low-frequency nonlinearity diagnosis

ABSTRACT

Electrochemical impedance spectroscopy (EIS) oriented methods are increasingly discussed and attempted in the analysis and diagnosis of the Lithium-ion battery (LIB). Yet, the parasitic, nonlinear and time-variant features of LIB pose challenges for their proper employment. To fill in the gap between the acquisition of EIS and its following utilization, it is essential to validate, calibrate and modify the raw EIS measurements. In this paper, theoretical background of such EIS preprocessing techniques based on the distribution of relaxation time (DRT) transform are closely discussed. An EIS validation approach alternative to the Kramers-Krönig relations is presented with mathematical rigor. To fix the high-frequency distortion, inductive correction for EIS is investigated. For the isolation or modification of particular kinetics, EIS data manipulation measures are proposed. Diagnosis of the low-frequency EIS is performed to reflect the extend of the induced nonlinearity and time-variance. The practicality and the benefits of these treatments are validated with commercial batteries, and they can well serve as routine checks for EIS. As the applications of EIS are going on-vehicle, online and dynamic, this paper seeks to supplement some valuable references for the effective preprocessing of EIS data prior to their critical usage.

1. Introduction

EIS technique is frequently used in the non-destructive analysis of various energy components [1], and plays a crucial part especially in characterizing the multi-physics of LIB [2–5]. It is also beneficial to apply EIS to the manufacturing quality management [6,7], the material characteristics evaluation [8], various states estimation or prediction [9–11] such as state of charge (SOC) and state of health (SOH), the internal temperature monitoring [12,13], the second-life utilization [14] and so on. Despite its simple working principle [15], the reliable and accurate acquisition of EIS can be tricky and calls for extra care [1].

Apart from the classical offline EIS, there are also new attempts to acquire the EIS data. By introducing direct current (DC) offset, battery

impedance monitoring during charge or discharge is enabled, and the diagnosis of battery can be realized by integrating such mechanism into the charging facility [16]. The first-order harmonic is generally emphasized for EIS, yet other harmonics, especially the second- and third-order, are also studied to extract the clues of LIB states. Specifically using high current rate to excite the nonlinear behavior of battery to a larger extend, ideas of the nonlinear frequency response analysis (NFRA) [17] and the nonlinear EIS (NLEIS) [18] are proposed. Combined with the electrochemical modeling, work in [19] analyzes the impedance of higher harmonics and finds helpful connections to the model parameters reflecting the internal states. Since the analysis of nonlinear features requires extra prior knowledge and theories, more efforts are urged to make them more useful [20]. Moreover, thermal control of LIB under

* Corresponding author.

E-mail address: wangdf@hit.edu.cn (D. Wang).

high current rate is also challenging [21]. Thus, compared to the approach with high-order harmonics, traditional EIS with the fundamental wave still finds more application scenarios, and is mainly addressed within this paper.

Traditional EIS test is low in efficiency and requires special equipment, which limits its use especially in on-vehicle applications. Research efforts are also invested to look for more feasible solutions. By careful design, the excitation and response of dynamic EIS (DEIS) contain multiple harmonics of interest, and the impedances at those frequencies can be extracted simultaneously in a single measurement, avoiding the shift of LIB states caused by the electrochemical dynamics. Yet, DEIS can only be obtained at frequencies that are integral multiples of the fundamental wave, and the SNR of higher harmonics is significantly reduced. Injecting the active excitations with the help of controllers such as the charger, the battery management system (BMS) and the electric motor controller, also proves applicability for the on-vehicle EIS measurement [22]. In addition, calculating the impedance passively with the operating current and voltage on a running electric vehicle is also proposed and discussed [23]. However, both of the active and the passive EIS still remain as prototype.

Through the analysis and interpretation of the obtained EIS, the electrochemical processes can be decoupled and the implicit clues can be found to guide the evaluation and optimization of LIB. Modeling with the electrochemical theory [24–26] and the equivalent circuit analogy [27–29] is generally used for the interpretation of EIS. Such methods first make hypothesis about the impedance of the LIB under investigation, then establish the impedance model, and finally obtain the underlying information by fitting into the EIS measurements. In order to eliminate the subjectivity of the interpretation and enable the in-depth analysis of EIS temporally, the idea of DRT is applied [30]. Although DRT remains an equivalent circuit-based method, its versatility are recognized as outstanding [31]. With the help of DRT, the time related evidences implied by the EIS is revealed, and the kinetics inside an electrochemical system can be visualized at a higher resolution. Some literatures try to attribute the DRT peaks to particular processes, and realize the estimation of the internal states for LIB [32,33]. For further interpretation, EIS should be validated first, and the most common approach is the Kramers-Krönig (K-K) relations. Validation using K-K is originally applied in the fields of optics and solid state physics [34]. As EIS prevails, it is also gradually adopted in the field of energy. DRT can not only be used as an interpretive tool for EIS, but also in this article, its potential in the validation, correction, manipulation, and diagnosis of EIS is unveiled.

The three fundamental requirements for EIS test are linearity, causality and stationarity [1]. Causality refers to the strict correspondence between a perturbation and its resulting response. Linearity requires that the input and output of a system satisfy the superposition principle. Stationarity implies time-invariance, and hence indicate that the inherent properties of the system do not change over time. With the experimental conditions controllable and the external properties measurable, causality can be essentially satisfied in EIS test. However, electrochemical systems, including LIBs, regularly suffer from nonlinearity and time-variance, and their deviation from the ideal linear time-invariant (LTI) system makes the last two requirements difficult to meet. By conducting incremental capacity analysis (ICA) [35], it is evident that the phase transformation of active materials or the open circuit voltage (OCV), which causes the time-varying chemical potential difference between electrodes, essentially dominates the nonlinearity of the LIB.

Based on the framework in [36], the relationship between the time-variant and -invariant features of LIB can be demonstrated more intuitively. The simplified model in Fig. 1 is constructed using micro-units of different phases under the spatial topology of LIB in [36], where {sldc} and {slda} are the solid phases of active material in cathode and anode, {cacei} and {cmsei} represent mixtures of cathode electrolyte interphase (CEI) film and solid electrolyte interphase (SEI)

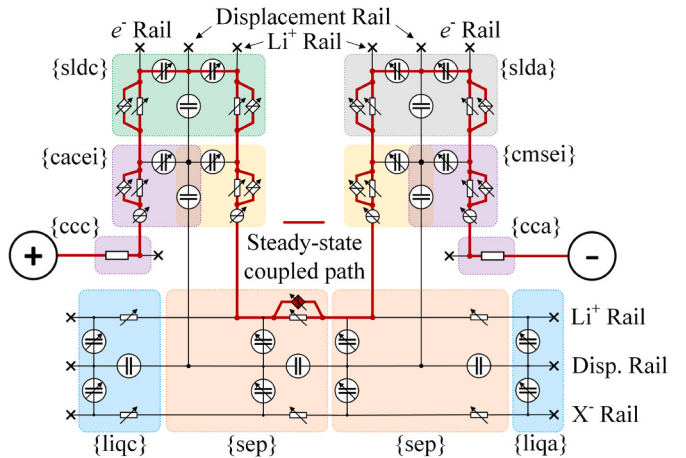


Fig. 1. Simplified equivalent circuits of LIB [36].

film with the conductive materials, and {liqc}, {sep} and {liqa} represent liquid phase in cathode, separator and anode. With the model shown in Fig. 1, the terminal voltage response at a given moment can be regarded as the sum of two parts, namely, the time-variant steady-state term represented by the current source and the time-invariant transient-state term by other components. The steady-state coupled path marked in red involves only the electron rail and part of the Lithium-ion rail. In discharge, electrons enter the path from the positive terminal through {cc} and {cacei}, and exit the path from the negative terminal through {cca} and {cmsei}. To maintain local neutrality of the solid and liquid phases, Li⁺'s leave {liqc}/{sep} and intercalate into {sldc}, while the same amount of Li⁺'s deintercalate from {slda} and enter {sep}/{liqa}, unifying the continuous current of external with the steady-state mass flow inside the LIB. This path produces the steady-state component of the terminal voltage, including the OCV corresponding to the chemical potentials of {sldc} and {slda} and the components associated with the electrochemical potential gradient. Other paths can only contribute to the transient components or the overpotentials. For example, since the anions X⁻ in {liqc}, {sep} and {liqa} do not participate in the insertion reactions and can only be transported among the liquid phases, the X⁻ rail contributes only transient components to the terminal voltage, which also applies to the boundary micro-units. The influence of the steady-state components might be overlooked, and thus introduces errors especially under highly dynamic conditions with large current. In Fig. 1, the time-variance of LIB is reflected by the steady-state coupled path and compromises the stationarity of EIS compromised. Therefore, for EIS measurements, especially those at low frequency, the amplitude of test current becomes a crucial factor [37,38], because the stationarity is undermined immediately when the current flows. Apart from the above-mentioned factors, there are also others causing extra nonlinearity and time-variance, such as the logarithmic relationship behind the interfacial reactions, the influence of temperature and the fractional-order properties of the porous electrode.

Whether acquired from the traditional EIS, the new DEIS, the active or the passive EIS, raw EIS measurements urge proper treatments before using them for further model fitting, process decoupling or state estimation. Without much prior knowledge, this article seeks to demonstrate some helpful preprocessing schemes using the DRT approach, and the contribution lies in the following aspects.

- (1) It is mathematically proved that the kernel of DRT inherently satisfies the K-K relations. Using DRT to validate EIS data can bring conveniences as well as overcome the numerical challenges of K-K.

- (2) Inductive characteristics of the test bench and the battery lead to drifting of EIS at high frequency. By compensating the high-frequency distortion, the influence of inductance is eliminated using DRT transform.
- (3) In order to remove, modify and isolate the electrochemical processes, an EIS data manipulation method based on DRT alteration is presented.
- (4) Quantitative correction of the low-frequency nonlinearity in EIS requires sufficient prior knowledge. In this paper, a qualitative diagnosis method for low-frequency EIS is proposed, and it can well reflect the nonlinearity and time-variance.

2. Experimental

To demonstrate the use of DRT for validation, correction, modification and diagnosis of EIS, traditional off-line EIS tests are arranged. The concerned test objects include dummy cell and two commercial batteries. To ensure the consistency in validation, both the dummy cell and the two commercial batteries are tested with 2 parallel samples. The dummy samples are red copper rod with 18 mm radius and 65 mm length. To ensure its contact with the test fixture, the surfaces at both ends are properly polished. The purpose of using dummy cell is to study the frequency response of the whole testbench without batteries. The two commercial batteries in 18650-case are named with S1 and S2 respectively, and their parameters are listed in [Table-1](#).

The test fixture adopts the same four-wire configuration as the electrochemical workstation, two for excitation path and two for sampling path. They are directly connected to the positive and negative terminals of the cell to minimize the coupled length between the current and sampling paths. The fixture adopts the typical BNC connectors, and the wirings between the electrochemical workstation and the fixture use coaxial cables. The shielding of the BNC connectors and the coaxial cables meets at the negative terminal of the battery. As discussed in [1, 39], factors other than batteries, such as the fixture and wiring layout, also affect the EIS test. Since the test fixture and the wirings can be reused, they should be carefully designed and verified before the experiments. Some hints for calibration and test design are given in [40]. The parasitic characteristics in the test bench cannot be completely eliminated, and reliable connections and good shielding mainly ensure the experimental consistency during test.

As described in Chapter I, test current is central in controlling the nonlinearity and non-stationarity of LIB, and thus the arranged experiments mainly focus on the analysis and verification of EIS with different currents. The test samples along with the fixture are placed in a climate chamber. To enrich the dataset for validation, commercial batteries are also tested at different SOCs.

Subject to the maximum current of the electrochemical workstation, the samples are tested according to the current sequences in [Table-2](#). For all samples, EIS tests are carried out at 25 °C with the frequency window of 10 m–100 kHz. Test of dummy samples is carried out continuously, while for the commercial ones, proper settling process is arranged. For current below C/10, the settling time between tests is 1 h, while for current above C/10, the settling time is extended to 6 h to ensure the thermal and electrochemical equilibrium of the sample, and to reduce the impact of operating history.

The test results of dummy samples are designed to investigate the

Table-1
Parameters of the batteries under test.

Cell name	S1	S2
Manufacturer	A123	Panasonic
Nominal capacity	1.1 Ah	3.2 Ah
Operating window	2.0 V–3.6 V	2.5 V–4.2 V
Chemistry	LFP	NCM
Number of samples	2	2

Table-2

Test current sequences.

Cell name	S1	S2
Current sequence	11 mA/22 mA/33 mA/110 mA/ 143 mA/253 mA/363 mA/689 mA/1018 mA/1345 mA/1674 mA/2000 mA	3 mA/30 mA/60 mA/90 mA/ 390 mA/690 mA/990 mA/1290 mA/1590 mA/1890 mA

inductive feature of the test bench under different currents, and to provide reference for the high-frequency distortion correction for the commercial batteries. EIS measurements of commercial batteries under different conditions are used for the validation of preprocessing schemes based on DRT transform. Since the raw data of parallel samples show good agreement with each other, only one set of data is used throughout this paper.

3. Theoretical

3.1. DRT transform and its inverse

Due to the ability to provide detailed electrochemical insights, method of DRT analysis receives increasing attention [1,31]. It can convert the impedance or transfer function of LTI system into the sum of infinite inertial elements with continuously distributed time constants as formula (1).

$$Z(\omega) - Z(+\infty) = \int_0^{+\infty} \frac{\gamma(\tau)}{1 + j\omega\tau} d\tau \quad (1)$$

where, ω is the angular velocity, $\gamma(\tau)$ is the distribution function, and τ is the time constant or the relaxation time.

For discrete DRT, (1) can be rewritten to (2), and the time constants can be rearranged in logarithmic order with $\tau_i = \lg \tau_i^*$, to accommodate the given number of frequencies per decade in EIS test.

$$Z(\omega_i) = R_\infty + \sum_1^{+\infty} \frac{\Gamma_i(\tau_i)}{1 + j\omega_i\tau_i} \quad (2)$$

where, $\Gamma_i(\tau_i) = \gamma(\tau)d\tau|_{\tau \rightarrow \tau_i}$.

DRT analysis relies on two key elements, namely the solving kernel and the solving method. For LIB, the solving kernel refers to the equivalent circuits suitable to simulate the full-cell impedance response. The solving method includes the solving objective, the type of solver, and the regularizing and weighing configuration. These aspects basically determine the solving procedures and the performance. Unlike the conventional equivalent circuit model or the mechanistic impedance model, the solving kernel of DRT is essentially free of prior knowledge, and if strictly speaking, only a small amount of intinction is required. The original DRT kernel includes the N-order RC structure. The impedance of a cluster of RCs only exists in the first quadrant of the Nyquist plot (The imaginary part is inversed, and this convention is used throughout this paper). To adapt to the real part shift of EIS, DC resistance term R_∞ is added. When the capacitor in an RC element is small enough to be interpreted as circuit break, RC is reduced to a resistor. This reveals the general relationship between the RC, RL element and the discrete resistor, capacitor and inductor. In addition to adding a DC resistance, DRT kernel's descriptive ability can also be improved by introducing other components and combinations, as shown in [Fig. 2](#). Low-frequency characteristics can be readily simulated by a discrete capacitor. Similar result can be achieved when the resistor in an RC element is so large that it is looked as circuit break, reducing the RC to a capacitor. Yet, adding a single capacitor is only helpful to improve the numerical stability of DRT solving when the imaginary parts of EIS grow faster than the real ones at low frequency, and can be improved. In addition, impedances such as the constant phase element (CPE) and the Warburg family can also be adopted. For the characterization of the

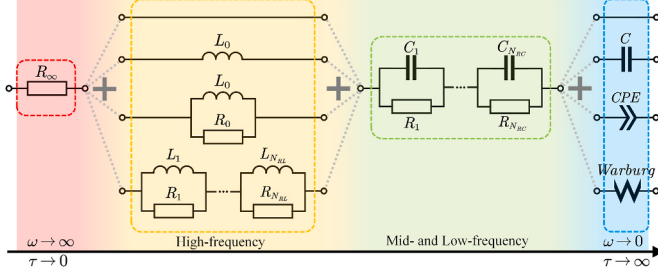


Fig. 2. Structures of the solving kernels.

inductance at high frequency, a discrete inductor, single RL element or a series of RL elements can be added, which is closely discussed in Chapter IV. Due to the regularization used in the DRT solving, variations between adjacent RC/RL elements are suppressed to obtain smoother distributions. Therefore, although RC and RL element can be reduced into pure inductance, capacitance, and resistance, it is still necessary to add discrete components to improve the effectiveness in numerical solving. Choosing among these kernels actually require little mechanistic understanding of the LIB. Mere considerations on the timescale and the contribution to the landscape of EIS is sufficient. In fact, collection of the solving kernels is small due to the brief physical implication of DRT.

The solving of distribution function by deconvoluting the EIS is to seek the best fit into the solving kernel. For this purpose, methods are proposed such as the Tikhonov regularization, Monte Carlo sampling, genetic algorithm, Fourier transform, Gaussian process regression, neural network and so on [41–45]. The DRT analysis essentially solves an ill-posed inverse problem [1] and different possible solutions can exist. By adopting the ridge regression, also known as the Tikhonov regularization, the reliability of numerical calculations is improved to yield consistent results with the potential pseudo peaks minimized. To evaluate the performance of the above numerical treatments, analytical distribution functions of specific impedance, such as CPE and finite length Warburg (FLW), can be used as reference [46,47]. Taking the simplest kernel in Fig. 2 as an example, the numerical solving of DRT is discussed as below.

For the kernel without inductor and low-frequency components, the impedance is written as (3).

$$Z(\omega) = R_{\infty} + \sum_{n=1}^{N_{RC}} \frac{\Gamma_{RC}(\nu_n)}{1 + j\omega\nu_n} \quad (3)$$

where, ν_n is the time constant of n th RC element, and the total number of RC element is N_{RC} .

Collecting the real and imaginary parts in (3) gives (4).

$$Z(\omega) = \left[R_{\infty} + \sum_{n=1}^{N_{RC}} \frac{\Gamma_{RC}(\nu_n)}{1 + (\omega\nu_n)^2} \right] - j \left[\sum_{n=1}^{N_{RC}} \frac{\omega\nu_n \Gamma_{RC}(\nu_n)}{1 + (\omega\nu_n)^2} \right] \quad (4)$$

For brevity, the DRT solving with respect to certain kernel can be written as (5). The distribution function can be obtained by solving vector X in (5), and (5) is the compact form of (5a).

$$\mathbf{A}X = \begin{bmatrix} \mathbf{Z}_{mea}^{\text{Re}} \\ \mathbf{Z}_{mea}^{\text{Im}} \end{bmatrix} \quad (5)$$

where, the bold symbol indicates a matrix or vector, and the EIS measurement \mathbf{Z}_{mea} has N_{mea} impedances expressed as $\mathbf{Z}_{mea} = \mathbf{Z}_{mea}^{\text{Re}} + j\mathbf{Z}_{mea}^{\text{Im}}$, and the superscripts represent the real and imaginary part respectively.

$$\begin{bmatrix} \mathbf{A}_{S1} & \mathbf{A}_{RC}^{\text{Re}} \\ \mathbf{A}_{S2} & \mathbf{A}_{RC}^{\text{Im}} \end{bmatrix} \begin{bmatrix} R_{\infty} \\ \Gamma_{RC}(\nu_1) \\ \vdots \\ \Gamma_{RC}(\nu_{N_{RC}}) \end{bmatrix} = \begin{bmatrix} Z_{mea}^{\text{Re}}(\omega_1) \\ \vdots \\ Z_{mea}^{\text{Re}}(\omega_{N_{EIS}}) \\ Z_{mea}^{\text{Im}}(\omega_1) \\ \vdots \\ Z_{mea}^{\text{Im}}(\omega_{N_{EIS}}) \end{bmatrix} \quad (5a)$$

where, $[\Gamma_{RC}(\nu_1) \dots \Gamma_{RC}(\nu_{N_{RC}})]^T$ can be shortened to vector Γ_{RC} , $\mathbf{A}_{S1} = [1 \dots 1]^T$, $\mathbf{A}_{S2} = [0 \dots 0]^T$,

The distribution function Γ_{RC} is solved with $(1+N_{RC})$ unknowns and $2 \cdot N_{EIS}$ equations. The number of solving points of DRT is relatively large, making (5) an under-determined solving problem, which can also be understood as an optimization problem. The various solving strategies mentioned above all seek the reliable solving of (5). Proper constraints should be present to search for the solution, and formula (6) is a typical constraint or optimization objective. As discussed in [48,49], the regularization strategy in (6) also bears the statistical significance.

$$\min_{\Gamma \geq 0} \{ \| \mathbf{W}^{\text{Re}} (\mathbf{Z}_{drt}^{\text{Re}} - \mathbf{Z}_{mea}^{\text{Re}}) \|_2^2 + \| \mathbf{W}^{\text{Im}} (\mathbf{Z}_{drt}^{\text{Im}} - \mathbf{Z}_{mea}^{\text{Im}}) \|_2^2 + \| \Lambda \Gamma \|_2^2 \} \quad (6)$$

where, separate weighing matrices \mathbf{W}^{Re} and \mathbf{W}^{Im} are used for real and imaginary parts, \mathbf{Z}_{drt} includes impedances of the chosen kernel calculated with a positive distribution function Γ , Λ is the regularization coefficient matrix, and the last penalty term $\Lambda \Gamma$ fulfills the regularization.

In addition to the solving kernel and the solving objective, the range and number of solving points are also to be assigned, namely the range of time constant ν and the size of N_{RC} . It is regular to assign the same frequency range as the measured EIS, yet it is also possible to expand or narrow the window as needed. The frequency sweeping of EIS ensures that all governing processes within the range of interest are reliably captured. At the upper and lower limits of the frequency window, existing process with similar time constants can also be reflected in the EIS. Thus, by appropriately expanding the window of DRT solving, these processes can also be recognized in DRT results.

The intuitive physical significance of DRT analysis can be explained by its kernel, i.e., the measured EIS is approximated with clusters of RC and RL elements, whose impedance are semi-arcs in the first and fourth quadrant of the Nyquist plot, respectively. The peak of each DRT corresponds to a cluster of RCs or RLs, whose time constants in the cluster follow a specific distribution. Behind each peak is an electrochemical process inside the LIB. The height of each peak indicates the significance of the corresponding kinetics, while its position indicates the acting window. It is worth noting that incomplete peaks similar to spectrum leakage can exist. They often imply that more kinetics can be expected outside the window, or probably the measurement noise.

Due to the perspective that the distribution function can be looked as a spectrum, the DRT analysis is renamed as DRT transform in this paper, and denoted by \mathfrak{D} . The DRT transform in (7) represents the procedure described above for solving the distribution function Γ with chosen kernel and solving method.

$$\Gamma = \mathfrak{D}_{kernel}^{\text{method}} (\mathbf{Z}_{mea}) \quad (7)$$

Similarly, the inverse DRT transform, denoted by \mathfrak{D}^{-1} , can also be defined as (8), which is the procedure of reconstructing EIS with a given distribution function Γ and kernel.

$$\mathbf{Z}_{idrt} = \mathfrak{D}^{-1}_{kernel}(\Gamma) \quad (8)$$

3.2. K-K property of the solving kernels

The K-K relations are the first to reveal the interrelation between the real and imaginary parts of the complex susceptibility [50,51]. Although

the original result is derived from the atomic gas model, the principle reflected by the K-K relations is independent of background, and universal in electrics, mechanics and acoustic systems. It describes the intrinsic relation within the LTI system, namely, the imaginary part of the transfer function or impedance can be inferred with the real part and vice versa. K-K is also available to verify the transfer function or impedance for cases where both real and imaginary parts are given, such as the EIS data of LIB. One derivation of K-K relations is given in [52]. The Sokhotski-Plemelj operator is first obtained with the help of the nascent delta function $\epsilon/[\pi(\omega^2 + \epsilon^2)]$, with equation (9) being one of its forms.

$$\frac{-j}{\omega - j\epsilon} = \pi\delta(\omega) - j\frac{\mathcal{P}}{\omega} \quad (9)$$

where, \mathcal{P} denotes the Cauchy principal value of the integral.

Then Fourier transform is performed for the causal function, and equation (10) with convolution operator is obtained. The tilde indicates the Fourier transform, where $H(\omega)$ is the Heaviside function.

$$\tilde{F}(\omega) = \frac{1}{2\pi} \tilde{H}(\omega) * \tilde{F}(\omega) \quad (10)$$

Bringing (9) into (10) yields (11).

$$\begin{aligned} \tilde{F}(\omega) &= \frac{1}{2\pi} \left[\pi\delta(\omega) - j\frac{\mathcal{P}}{\omega} \right] * \tilde{F}(\omega) \\ &= \frac{1}{2} \delta(\omega) * \tilde{F}(\omega) - j \frac{1}{2\pi} \left(\frac{\mathcal{P}}{\omega} \right) * \tilde{F}(\omega) \end{aligned} \quad (11)$$

(11) can be reduced to (12).

$$\tilde{F}(\omega) = -j \frac{1}{\pi} \left(\frac{\mathcal{P}}{\omega} \right) * \tilde{F}(\omega) \quad (12)$$

Isolating the real and imaginary parts of (12) with $\tilde{F} = \tilde{F}^{\text{Re}} + j\tilde{F}^{\text{Im}}$ gives one form of the K-K relations as (13).

$$\begin{cases} \tilde{F}^{\text{Re}}(\omega) = \frac{2\mathcal{P}}{\pi} \int_0^{+\infty} \frac{\tilde{F}^{\text{Im}}(s)}{\omega - s} ds \\ \tilde{F}^{\text{Im}}(\omega) = -\frac{2\mathcal{P}}{\pi} \int_0^{+\infty} \frac{\tilde{F}^{\text{Re}}(s)}{\omega - s} ds \end{cases} \quad (13)$$

It is notable that (13) can also be written in the form of (14), namely the Hilbert transform denoted by \mathcal{H} .

$$\begin{cases} \tilde{F}^{\text{Re}} = \mathcal{H}(\tilde{F}^{\text{Im}}) \\ \tilde{F}^{\text{Im}} = -\mathcal{H}(\tilde{F}^{\text{Re}}) \end{cases} \quad (14)$$

The above derivations prove that the K-K relations exist as a special form of Hilbert transform, and the real and imaginary parts can be deduced from each other for LTI systems satisfying causality. Such connection can be more generally written as formula (15).

$$Z_{LTI} = -j\mathcal{H}(Z_{LTI}) \leftrightarrow \mathcal{H}(Z_{LTI}) = jZ_{LTI} \quad (15)$$

Regardless of the general conclusion in (15), the Hilbert transform is performed by solving the limit of primitive G as in (16).

$$\begin{aligned} \mathcal{H}(Z) &= \frac{1}{\pi} [G(\omega, \omega - \epsilon)|_{\epsilon \rightarrow 0^+} - G(\omega, \omega + \epsilon)|_{\epsilon \rightarrow 0^+} \\ &\quad + G(\omega, l)|_{l \rightarrow \infty} - G(\omega, -l)|_{l \rightarrow \infty}] \end{aligned} \quad (16)$$

where, $G(\omega, s) = \int \frac{Z(s)}{\omega - s} ds$.

Although the K-K relations defined in (13) is simple in form, it suffers from problems in practical application: (a) treatment of the singularity in the integral needs extra care, and the calculation near the singularity has great influence on the final results, and (b) the number of frequency points is limited and only a small number of measurements can be used. The problems limit the further application of K-K. Currently, among many EIS researches, only few of them use K-K to verify the

experimental data. As mentioned earlier, the three main requirements of the EIS test can be potentially compromised. Therefore, it is necessary to analyze and verify the original EIS data before their following usage. It is possible to improve the K-K relations numerically, yet the effect is limited. This section aims to present an alternative to K-K validation based on the idea of DRT by analyzing the basic RC and RL element of the solving kernel. The primitive of RC and RL elements are constructed in (17) and (18) respectively.

$$\begin{aligned} G_{RC}(\omega, s) &= \int \frac{Z_{RC}}{\omega - s} ds = \int \frac{1}{(1 + j\tau s)(\omega - s)} ds \\ &= \frac{2 \arctan(\tau s) + 2j \ln(-\omega + s) - j \ln(1 + \tau^2 s^2)}{-2j + 2\tau\omega} \end{aligned} \quad (17)$$

$$\begin{aligned} G_{RL}(\omega, s) &= \int \frac{Z_{RL}}{\omega - s} ds = \int \frac{j\tau\omega}{(1 + j\tau s)(\omega - s)} ds \\ &= \frac{2 \arctan(\tau s) + 2\tau\omega \ln(-\omega + s) - j \ln(1 + \tau^2 s^2)}{2j - 2\tau\omega} \end{aligned} \quad (18)$$

Regardless of the complexity in calculation, Hilbert transform of RC and RL impedance can be resolved using (16)-(18), and finally (19) and (20) can be yielded. By comparing the conclusions of (14) and (15), the correctness of (19) and (20) can also be conveniently checked.

$$\mathcal{H}(Z_{RC}) = \mathcal{H}\left(\frac{1}{1 + j\tau\omega}\right) = \frac{j}{1 + j\tau\omega} = jZ_{RC} \quad (19)$$

$$\mathcal{H}(Z_{RL}) = \mathcal{H}\left(\frac{j\tau\omega}{1 + j\tau\omega}\right) = \frac{-\tau\omega}{1 + j\tau\omega} = jZ_{RL} \quad (20)$$

Considering the connection between the K-K relations and the Hilbert transform, single RC and RL element can satisfy K-K relations unconditionally. Thus, for the solving kernels with RCs and RLs in series, the K-K relations can still hold, and the impedance Z_{drt} generated by the DRT transform naturally conforms to the K-K validation. Compared to the traditional K-K validation, DRT-based alternative avoids the problem of singularity. Since the DRT transform can yield an optimal solution regarding the distribution of time constants, new EIS data points conforming to that distribution can be augmented based on the original EIS data. To summarize, while deconvoluting the EIS with DRT transform, without extra effort, on the one hand can the validity of the EIS data be verified, and on the other hand, mutual deduction of real and imaginary parts and prediction of the impedances outside the measuring frequency window can also be realized.

4. Results and discussion

In this section, the DRT transform will be used to perform the high-frequency correction, the data validation, the shape manipulation, and the low-frequency diagnosis for EIS raw measurements.

4.1. Correction of high-frequency distortion

With the test frequency higher than kilohertz, the EIS will enter the fourth quadrant of the Nyquist plot, where the inductive feature of the test bench and the battery dominates the trend of EIS. In order to focus on the electrochemical process and characteristics inside the battery, DRT transform can be used to eliminate the inductive factors and realize the correction for the high-frequency distortion of EIS. The resulting EIS curve locates itself entirely in the first quadrant of the Nyquist plot and fully satisfies the K-K relations, which is conducive for further analysis and interpretation of EIS.

Fig. 3(a) shows the EIS of dummy cell under different currents. The results reflect the overall impedance response of the circuit composed of the dummy cell, the test equipment, the wirings and the fixture. The EIS curves lie in the fourth quadrant of the Nyquist plot, showing mostly the inductive feature. For test with 3 mA, large fluctuations can be seen due to the low SNR. As the current increases, the EIS curve becomes

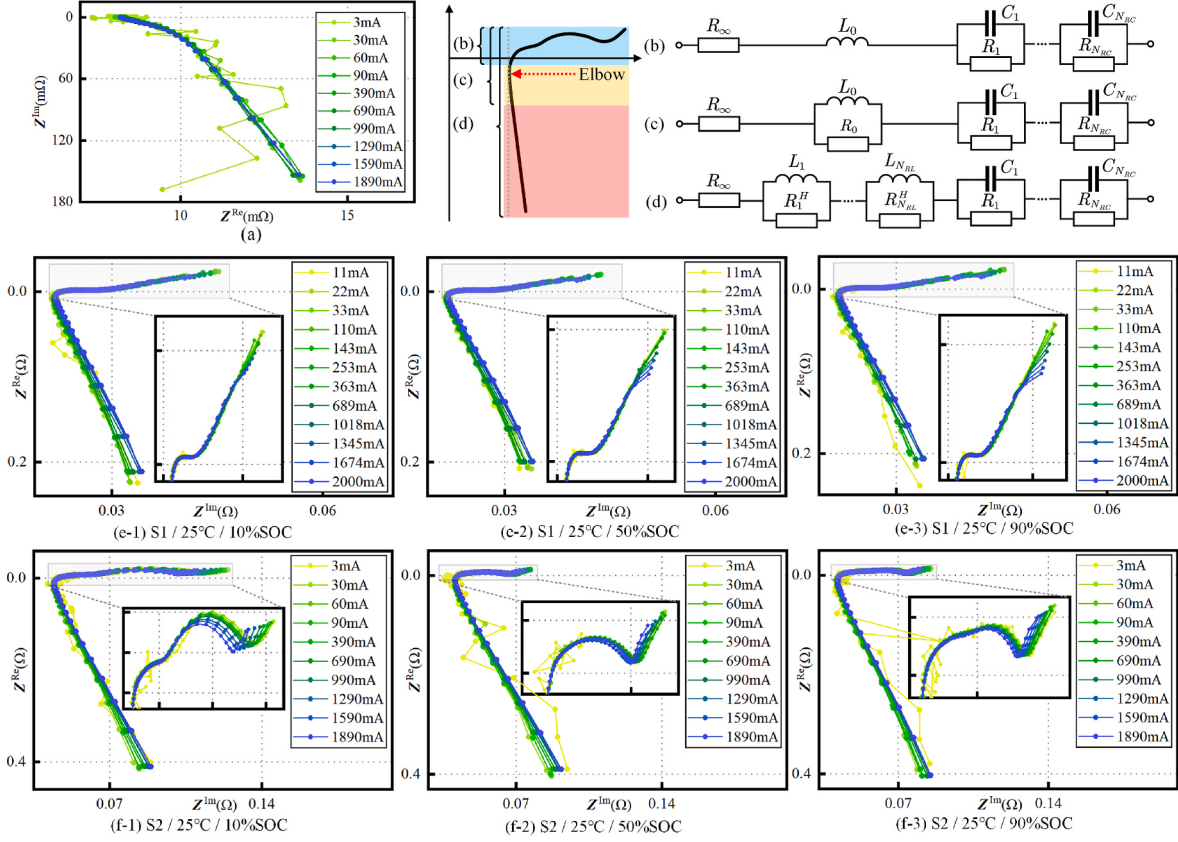


Fig. 3. (a) Inductive feature of the test bench, (b–d) the solving kernels used for high-frequency distortion correction, (e–f) raw EIS of S1 and S2 cell.

smoother in shape. Seeing that the impedance change caused by different current is very small, it is assumed that the parasitic inductance of the test bench is basically constant and insensitive to current.

Different solving kernels can be used for the high-frequency distortion correction. The applicability of the three kernels in Fig. 3(b–d) along with their correction procedures are discussed as follows.

For the kernel in Fig. 3(b) composed of \$R_\infty\$, \$L_0\$ and \$N_{RC}\$ RC elements, its impedance can be written as (21).

$$Z(\omega) = \left[R_\infty + \sum_{n=1}^{N_{RC}} \frac{\Gamma_{RC}(\nu_n)}{1 + (\omega\nu_n)^2} \right] + j \left[\omega L_0 - \sum_{n=1}^{N_{RC}} \frac{\omega\nu_n \Gamma_{RC}(\nu_n)}{1 + (\omega\nu_n)^2} \right] \quad (21)$$

Rewriting (21) into the form of (5a) yields (22).

$$\begin{bmatrix} A_{S1} & A_{S2} & A_{RC}^{\text{Re}} \\ A_{S2} & A_{S3} & A_{RC}^{\text{Im}} \end{bmatrix} \begin{bmatrix} R_\infty \\ L_0 \\ \Gamma_{RC} \end{bmatrix} = \begin{bmatrix} Z_{\text{mea}}^{\text{Re}} \\ Z_{\text{mea}}^{\text{Im}} \end{bmatrix} \quad (22)$$

where, \$A_{S3} = [\omega_1 \dots \omega_{N_{RC}}]^T\$.

For the kernel in Fig. 3(c), the inductance is replaced with the \$R_0L_0\$ element, and its impedance is (23).

$$Z(\omega) = \left[R_\infty + \frac{\omega^2 \mu_0 L_0}{1 + (\omega\mu_0)^2} + \sum_{n=1}^{N_{RC}} \frac{\Gamma_{RC}(\nu_n)}{1 + (\omega\nu_n)^2} \right] + j \left[\frac{\omega L_0}{1 + (\omega\mu_0)^2} - \sum_{n=1}^{N_{RC}} \frac{\omega\nu_n \Gamma_{RC}(\nu_n)}{1 + (\omega\nu_n)^2} \right] \quad (23)$$

Rewriting (23) into the form of (22) yields (24).

$$\begin{bmatrix} A_{S1} & A_{RL0}^{\text{Re}} & A_{S2} & A_{RC}^{\text{Re}} \\ A_{S2} & A_{S3} & A_{RL0}^{\text{Im}} & A_{RC}^{\text{Im}} \end{bmatrix} \begin{bmatrix} R_\infty \\ L_0 \\ \mu_0 \\ \Gamma_{RC} \end{bmatrix} = \begin{bmatrix} Z_{\text{mea}}^{\text{Re}} \\ Z_{\text{mea}}^{\text{Im}} \end{bmatrix} \quad (24)$$

$$\text{where, } A_{RL0}^{\text{Re}} = \begin{bmatrix} \frac{\omega_1^2 \mu_0}{1 + (\omega_1 \mu_0)^2} & \dots & \frac{\omega_{N_{\text{mea}}}^2 \mu_0}{1 + (\omega_{N_{\text{mea}}} \mu_0)^2} \end{bmatrix}^T, \quad \text{and} \quad A_{RL0}^{\text{Im}} = \begin{bmatrix} \frac{\omega_1}{1 + (\omega_1 \mu_0)^2} & \dots & \frac{\omega_{N_{\text{mea}}}}{1 + (\omega_{N_{\text{mea}}} \mu_0)^2} \end{bmatrix}^T.$$

For the kernel in Fig. 3(d) composed of \$M_{RL}\$ RL elements, its impedance can be written as (25).

$$Z(\omega) = \left[R_\infty + \sum_{m=1}^{M_{RL}} \frac{(\omega\mu_m)^2 \Gamma_{RL}(\mu_m)}{1 + (\omega\mu_m)^2} + \sum_{n=1}^{N_{RC}} \frac{\Gamma_{RC}(\nu_n)}{1 + (\omega\nu_n)^2} \right] + j \left[\sum_{m=1}^{M_{RL}} \frac{\omega\mu_m \Gamma_{RL}(\mu_m)}{1 + (\omega\mu_m)^2} - \sum_{n=1}^{N_{RC}} \frac{\omega\nu_n \Gamma_{RC}(\nu_n)}{1 + (\omega\nu_n)^2} \right] \quad (25)$$

Rewriting (25) into the form of (24) yields (26).

$$\begin{bmatrix} A_{S1} & A_{RL}^{\text{Re}} & A_{RC}^{\text{Re}} \\ A_{S2} & A_{RL}^{\text{Im}} & A_{RC}^{\text{Im}} \end{bmatrix} \begin{bmatrix} R_\infty \\ \Gamma_{RL} \\ \Gamma_{RC} \end{bmatrix} = \begin{bmatrix} Z_{\text{mea}}^{\text{Re}} \\ Z_{\text{mea}}^{\text{Im}} \end{bmatrix} \quad (26)$$

$$\text{where, } A_{RL}^{\text{Re}} = \begin{bmatrix} \frac{(\omega_1 \mu_1)^2}{1 + (\omega_1 \mu_1)^2} & \dots & \frac{(\omega_1 \mu_{M_{RL}})^2}{1 + (\omega_1 \mu_{M_{RL}})^2} \\ \vdots & \ddots & \vdots \\ \frac{(\omega_{N_{\text{mea}}} \mu_1)^2}{1 + (\omega_{N_{\text{mea}}} \mu_1)^2} & \dots & \frac{(\omega_{N_{\text{mea}}} \mu_{M_{RL}})^2}{1 + (\omega_{N_{\text{mea}}} \mu_{M_{RL}})^2} \end{bmatrix}, \text{ and}$$

$$A_{RL}^{\text{Im}} = \begin{bmatrix} \frac{\omega_1\mu_1}{1 + (\omega_1\mu_1)^2} & \dots & \frac{\omega_1\mu_{M_{RL}}}{1 + (\omega_1\mu_{M_{RL}})^2} \\ \vdots & \ddots & \vdots \\ \frac{\omega_{N_{mea}}\mu_1}{1 + (\omega_{N_{mea}}\mu_1)^2} & \dots & \frac{\omega_{N_{mea}}\mu_{M_{RL}}}{1 + (\omega_{N_{mea}}\mu_{M_{RL}})^2} \end{bmatrix}.$$

The raw EIS curves of the two commercial batteries with different currents are shown in Fig. 3(e–f). Only results of one parallel sample are used. The divergence of the high-frequency impedance is more serious than that of the dummy cell in Fig. 3(a), implying that the battery itself

also exhibits inductive features with respect to current at high frequency.

The three kernels in Fig. 3(b–d) are used to carry out DRT transform of the EIS data respectively, and the simplest kernel in Fig. 2 is used to carry out the inverse DRT transform, so that the EIS reconstructed without inductance can be obtained. The three solving kernels can be used for different frequency ranges. The kernel in Fig. 3(b) is suitable for cases where the high-frequency impedance stops before the elbow due to that the discrete inductor yields an impedance perpendicular to the real

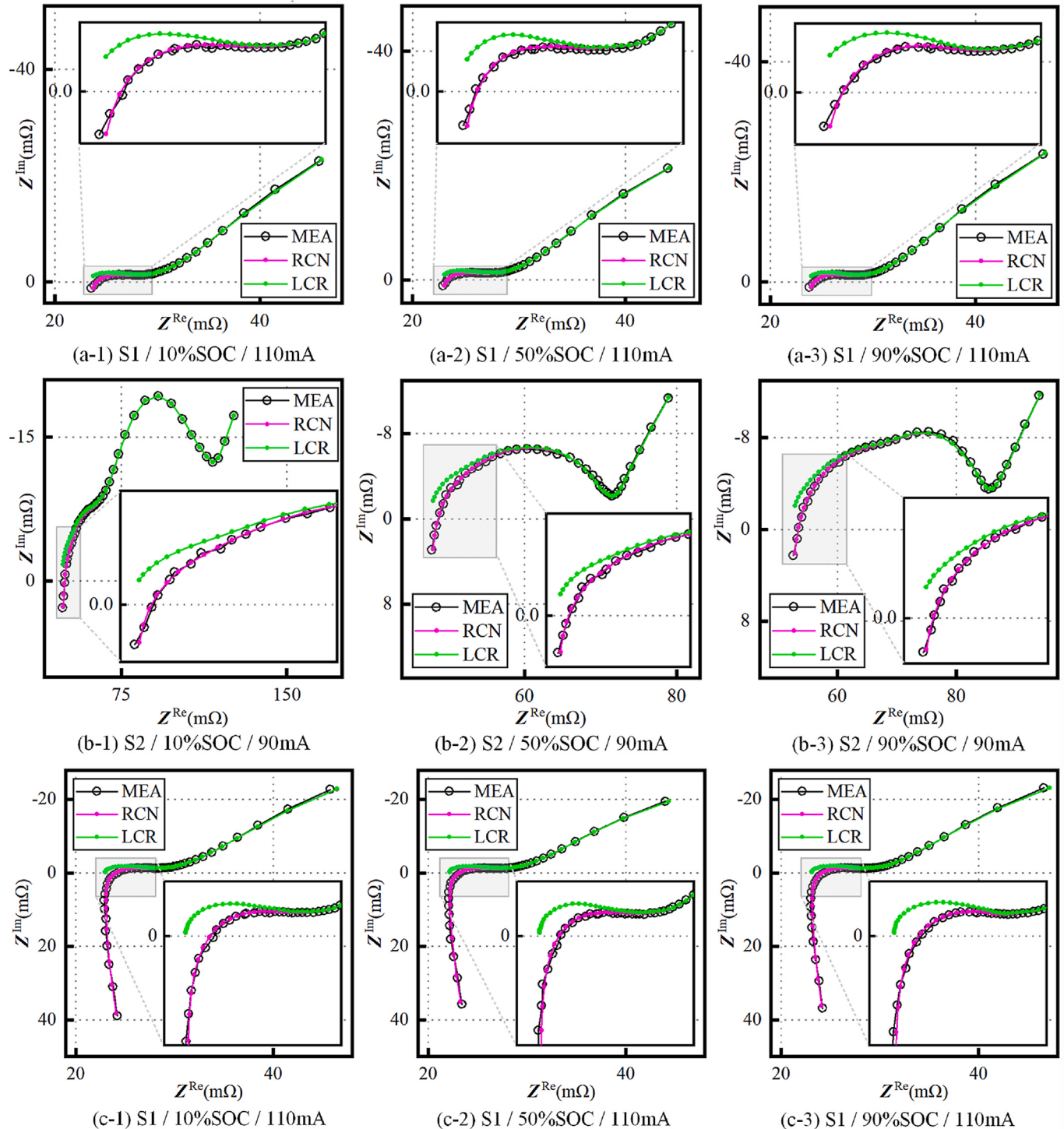


Fig. 4. (a–b) High-frequency correction with the solving kernel in Fig. 3(b), (c–d) High-frequency correction with the solving kernel in Fig. 3(c), (e–f) High-frequency correction with the solving kernel in Fig. 3(d).

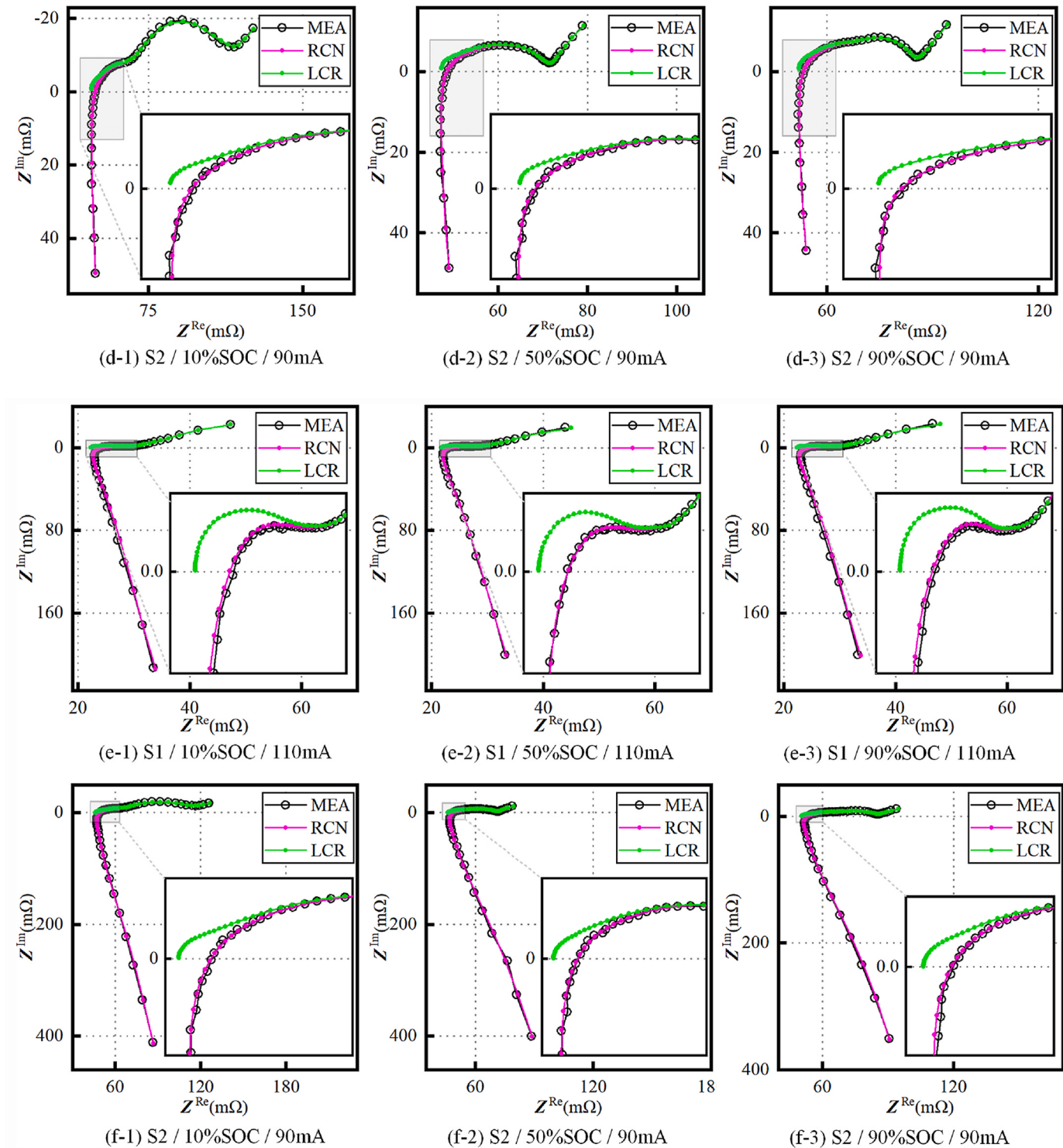


Fig. 4. (continued).

axis in the fourth quadrant. The kernel in Fig. 3(c) is suitable for scenarios where an arc-like impedance is present, considering that an RL element appears as a semi-circle in the fourth quadrant. The kernel in Fig. 3(d) can form a good fit for higher frequencies, as RC and RL elements can well simulate the impedance in both the first and the fourth quadrant. Therefore, these three kernels can realize the inductive correction of EIS in the appropriate high-frequency range as suggested in Fig. 3(b-d).

Fig. 4 compares the original EIS (MEA), the reconstructed EIS using

given kernels (RCN), and the reconstructed as well as inductance-corrected EIS using the simplest kernel in Fig. 2 (LCR), where EIS of the two commercial batteries under different SOCs of 10%, 50% and 90% are adopted. Validations in this section focus on the high-frequency region of EIS, and corresponding illustrations in Fig. 4 use the same EIS with different frequency windows, namely, 10 mHz~1 kHz for Fig. 4 (a-b), 10 mHz~10 kHz for Fig. 4(c-d) and 10 mHz~100 kHz for Fig. 4 (e-f). The reconstructed EISs (RCN) obtained using inverse DRT transform are in good agreement with the original EIS data (MEA). It is also

worth noting that the RCN curves are smoother than the MEA curves, and with the theoretical background in Section 2.1, the RCN curves can be understood as the least-square filtering of the MEA curves. The LCR curves come from the RCN curves with the inductive components removed, which can be used to facilitate the analysis of EIS.

Fig. 5(a) shows the two distribution functions of RC and RL for the solving kernel in Fig. 3(d), which is rarely discussed. The DRT of the RL elements shows a peak at much higher frequency, which depicts the inductive features in the high-frequency region of EIS. Interestingly, the shape of the high-frequency DRT peak of RL elements resembles that of the low-frequency peak of RC elements in shape, except for the symmetry. Analogous to the low-frequency ones, it may be viable to develop a new impedance to describe the high-frequency inductance for the EIS.

Fig. 5(b) shows the EISs measured with different currents from one sample of S1 at 50%SOC along with their reconstructed curves. The curves are properly rearranged along real axis for better view. It can be seen that even if the test current varies in a wide range, the reconstructed EIS in the high-frequency range can still show close agreement with the raw EISs, which proves that the high-frequency correction of EIS can be well achieved without prior knowledge, regardless of the existing current-related terms.

4.2. Validation of the raw EIS data

Viewed from the K–K relations or the Hilbert transform, validation of EIS mainly aims to mutually infer and compare its real and imaginary parts. The larger the gap between the inferred impedance and the actual one, the higher the deviation of the data from the three basic requirements of the EIS test, indicating a worse validity of the raw data as well as the inappropriateness for subsequent usage. EIS data validation also requires a suitable selection among known solving kernels of DRT, and the three situations described in Section 4.1 can come to the aid. To demonstrate the DRT-based EIS validation, kernel Fig. 3(b) is chosen. In order to make up for the error of the inferred imaginary parts at low frequencies, a discrete capacitor C_0 is added to this kernel, which is especially beneficial for EIS without asymptotic behavior [53].

The validation of EIS data need not to solve the optimal DRT by minimizing the collective deviation from both the real and imaginary parts, and requires a different procedure from the DRT transform defined by (5) and (6). When inferring the imaginary and real part through the raw EIS, two sets of distribution functions for the same kernel are expected, as defined in (27), where the vector \mathbf{T} denotes the sequence of time constants. For an ideal LTI system, $\mathbf{I}^{\text{Re}}(\mathbf{T}) = \mathbf{I}^{\text{Im}}(\mathbf{T})$ holds apparently.

$$\begin{cases} \mathbf{I}^{\text{Re}}(\mathbf{T}) = \mathfrak{D}|_{\text{kernel}}^{\text{method}}(\mathbf{Z}_{\text{mea}}^{\text{Re}}) \\ \mathbf{I}^{\text{Im}}(\mathbf{T}) = \mathfrak{D}|_{\text{kernel}}^{\text{method}}(\mathbf{Z}_{\text{mea}}^{\text{Im}}) \end{cases} \quad (27)$$

The problems for separate DRT transforms of real and imaginary parts are respectively defined in (28) and (29). \mathbf{I}^{Re} in (27) corresponds

to $\mathbf{I}_{\text{RC}}^{\text{Re}}$ and $\mathbf{I}_{\text{RL}}^{\text{Re}}$ in (28), and \mathbf{I}^{Im} corresponds to $\mathbf{I}_{\text{RC}}^{\text{Im}}$ and $\mathbf{I}_{\text{RL}}^{\text{Im}}$ in (29).

$$\begin{bmatrix} \mathbf{A}_{\text{SI}} & \mathbf{A}_{\text{RL}}^{\text{Re}} & \mathbf{A}_{\text{RC}}^{\text{Re}} \end{bmatrix} \begin{bmatrix} R_{\infty} \\ \mathbf{I}_{\text{RL}}^{\text{Re}} \\ \mathbf{I}_{\text{RC}}^{\text{Re}} \end{bmatrix} = \mathbf{Z}_{\text{mea}}^{\text{Re}} \quad (28)$$

$$\begin{bmatrix} \mathbf{A}_{\text{S4}} & \mathbf{A}_{\text{RL}}^{\text{Im}} & \mathbf{A}_{\text{RC}}^{\text{Im}} \end{bmatrix} \begin{bmatrix} 1/C_0 \\ \mathbf{I}_{\text{RL}}^{\text{Im}} \\ \mathbf{I}_{\text{RC}}^{\text{Im}} \end{bmatrix} = \mathbf{Z}_{\text{mea}}^{\text{Im}} \quad (29)$$

where, $\mathbf{A}_{\text{S4}} = [-1/\omega_1 \dots -1/\omega_{N_{\text{RC}}}]^T$.

For the solving of (27), two optimization conditions for DRT transforms are given as (30) and (31) respectively.

$$\min_{\mathbf{I}^{\text{Re}} \geq 0} \{ \| \mathbf{W}^{\text{Re}} (\mathbf{Z}_{\text{drt}}^{\text{Re}} - \mathbf{Z}_{\text{mea}}^{\text{Re}}) \|_2^2 + \| \mathbf{A}^{\text{Re}} \mathbf{I}^{\text{Re}} \|_2^2 \} \quad (30)$$

$$\min_{\mathbf{I}^{\text{Im}} \geq 0} \{ \| \mathbf{W}^{\text{Im}} (\mathbf{Z}_{\text{drt}}^{\text{Im}} - \mathbf{Z}_{\text{mea}}^{\text{Im}}) \|_2^2 + \| \mathbf{A}^{\text{Im}} \mathbf{I}^{\text{Im}} \|_2^2 \} \quad (31)$$

By inverse DRT transforming the two sets of the distribution functions obtained from (27) as given in (32), the inferred impedance $\mathbf{Z}_{\text{vld}} = \mathbf{Z}_{\text{vld}}^{\text{Re}} + j\mathbf{Z}_{\text{vld}}^{\text{Im}}$, corresponding to the raw EIS measurements, can be obtained.

$$\begin{cases} \mathbf{Z}_{\text{vld}}^{\text{Re}} = \mathfrak{D}^{-1}|_{\text{kernel}}(\mathbf{I}^{\text{Im}}(\mathbf{T})) + R_{\infty} \\ \mathbf{Z}_{\text{vld}}^{\text{Im}} = \mathfrak{D}^{-1}|_{\text{kernel}}(\mathbf{I}^{\text{Re}}(\mathbf{T})) \end{cases} \quad (32)$$

The differences between \mathbf{Z}_{vld} and \mathbf{Z}_{mea} can be quantified using particular methods, or the EIS curves can be intuitively compared as shown in Fig. 6, where the impedances labeled as ‘Rtol’ consist of the raw real parts and their inferred imaginary parts, which is $\mathbf{Z}_{\text{Rtol}} = \mathbf{Z}_{\text{mea}}^{\text{Re}} + j\mathbf{Z}_{\text{vld}}^{\text{Im}}$, while the ones labeled as ‘ItoR’ consist of the raw imaginary parts and their inferred real parts, which is $\mathbf{Z}_{\text{ItoR}} = \mathbf{Z}_{\text{vld}}^{\text{Re}} + j\mathbf{Z}_{\text{mea}}^{\text{Im}}$.

It can be seen from Fig. 6 that as the current increases, the EIS curves with inferred real or imaginary parts (‘Rtol’ and ‘ItoR’) deviates more and more from the raw EIS curve (MEA), especially in the low-frequency region, yet they match quite well in the mid- and high-frequency region. At a lower current, although large fluctuations exist due to low SNR, the three curves show relatively good agreement with each other. Via the intuitive comparison in the Nyquist plot, the range and the degree of the defected EIS data are self-explanatory, providing a feasible scheme for the validation of EIS data. The demonstrated scheme can not only circumvent the numerical dilemma of the traditional K–K validation, but also provide conveniences in densifying the sparse EIS measurements as well as predicting impedance outside the frequency window.

4.3. Manipulation of the EIS data

As described in Chapter II, the relaxation time distribution implied

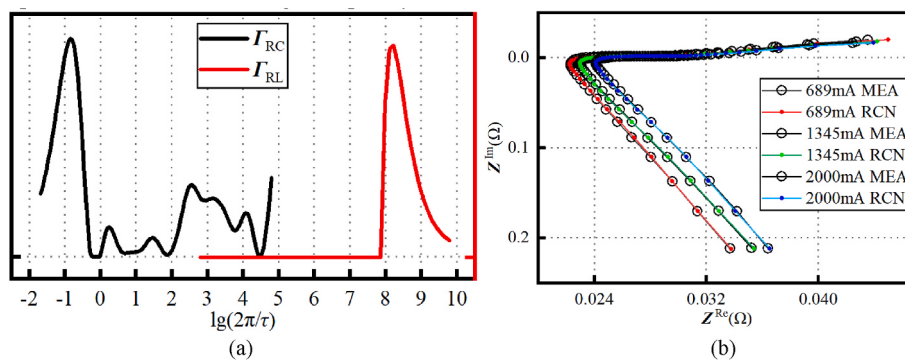


Fig. 5. (a) DRT of RC and RL elements, (b) EIS fitting results with different currents for S1 at 50%SOC.

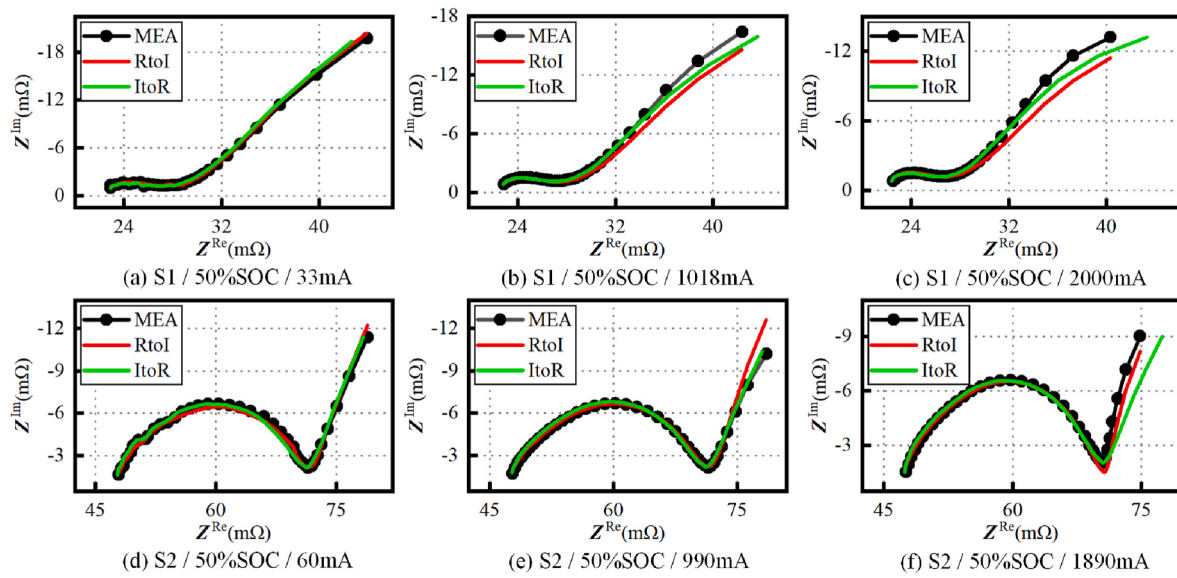


Fig. 6. EIS validation results.

by EIS data can be extracted by DRT transform. Given its clear physical implication, it is possible to modify the electrochemical processes for the manipulation of EIS data. Such modification includes the extraction, alteration, and removal of impedance fingerprints for specific electrochemical process. As shown in Fig. 5(a), the distribution obtained is a spectrum with identifiable peaks. Each peak refers to a specific kinetics within the LIB and can in fact be attributed to particular kinetics [32, 33]. Instead of interpreting the DRT peaks, this section presents the alteration of EIS curve by modifying the shape of DRT peaks, such as height, width, and position, to change the property of particular process. For peaks that are not preferentially concerned or considered insignificant, simple deletion is performed to remove distractions, so that the concerned collection of electrochemical processes can be focused. Indeed, it is also possible to carry out more meticulous operations on the distribution function, such as to fit and correct the shape of each peak by using the analytical distribution of theoretical impedance, so as to improve the consistency between the EIS data and the relevant theories. This can also provide some ideas for the state estimation and prediction based on EIS. With the obtained distributions in different conditions, the raise or shift of certain DRT peak can well indicate the aging, SOC and safety state of the battery. By means of off-line calibration and EIS data manipulation, it is possible to accurately predict the impedance behavior under dynamics.

DRT-based EIS data manipulation basically modifies the underlying parameters of the solving kernel, and the high-frequency inductance correction described in Section 4.1 is in fact a similar operation as such, with the inductance value cleared to zero. The EIS data manipulation are demonstrated according to the following three realistic needs: (a) Generally, the features corresponding to the high-frequency EIS exists less in the actual operation, and the mid- and low-frequency regions are emphasized, (b) in order to focus on the kinetics corresponding to the dynamic overpotentials, the low-frequency region of the EIS is excluded, (c) the mid-frequency region of the EIS changes significantly during aging, and the impedance response corresponding to this region is isolated.

The procedures of EIS data manipulation are introduced as follows. Firstly, DRT transform of EIS measurements is carried out with specific solving kernel and solving method as given in (33).

$$\Gamma(\mathbf{T}) = \mathfrak{D}|_{\text{kernel}}^{\text{method}}(\mathbf{Z}_{\text{mea}}) \quad (33)$$

Then, the obtained distribution function $\Gamma(\mathbf{T})$ is modified as demand to $\Gamma^*(\mathbf{T})$. Finally, inverse DRT transform is performed with the same

kernel and the new distribution $\Gamma^*(\mathbf{T})$ as input, as shown in (34) and (35), and the manipulated EIS \mathbf{Z}_{mp}^* is obtained.

$$\mathbf{Z}_{\text{mp}}^* = \mathfrak{D}^{-1}|_{\text{kernel}}(\Gamma^*(\mathbf{T})) \quad (34)$$

$$\mathbf{Z}_{\text{mp}} = \mathfrak{D}^{-1}|_{\text{kernel}}(\Gamma^*(\mathbf{T})) + \sum [\Gamma(\mathbf{T}) - \Gamma^*(\mathbf{T})] \quad (35)$$

The treatments in (34) and (35) provide different offsets for the real part of the manipulated EIS, which can also be understood as two types of alignment. The real part of the manipulated EIS using (34) is aligned to the original EIS by the highest frequency, while using (35) realizes alignment by the lowest frequency. EIS data manipulation using (35) implies that the removal of a DRT peak reduces the corresponding cluster of RC elements to resistors, rather than eliminates the whole cluster.

Using the inductance-corrected EIS of cell S2 at 10%SOC, Fig. 7 shows the manipulated EIS curves in the three situations (a)~(c) raised above. For each situation, two examples are given with their distribution functions and the resulting EISs. To conveniently compare the manipulated EIS, labeled as PM, with the inductance-corrected EIS, labeled as LCR, Fig. 7(a) and (c) adopt the EIS reconstruction in (35), while Fig. 7(b) in (34). From the results in Fig. 7, manipulation of the EIS data as well as the electrochemical process on the basis of the original EIS is realized by altering the original DRT, labeled as ORG, which enables the flexible and kinetics-oriented modification of the raw EIS.

4.4. Diagnosis of the low-frequency EIS

As analyzed in Chapter I, the mid- and low-frequency regions of EIS are susceptible to nonlinearity and internal states variation. Significant impedance drift can be seen in Fig. 3(e–f) for both commercial batteries when tested with different currents. For LPF S1, different currents mainly affect the tail of low-frequency region of the EIS, while for NCM S2, the impact of the growing current extends to the mid-frequency region, and the impedances above several Hertz are notably affected. In addition, the influence of current on impedance also presents inconsistency under different SOCs. Thus, it is conceivable that the EIS analysis under different test currents, especially at low frequencies, is highly dependent on prior knowledge. The low- and mid-frequency EIS mainly reflect the solid and liquid phase diffusion, the interfacial reaction and the material phase transformation. For the influence of phase transformation, an extreme example with OCV can be analyzed. Assuming that the excitation current $I(t)$ is close to zero, its period T_{exc} close to

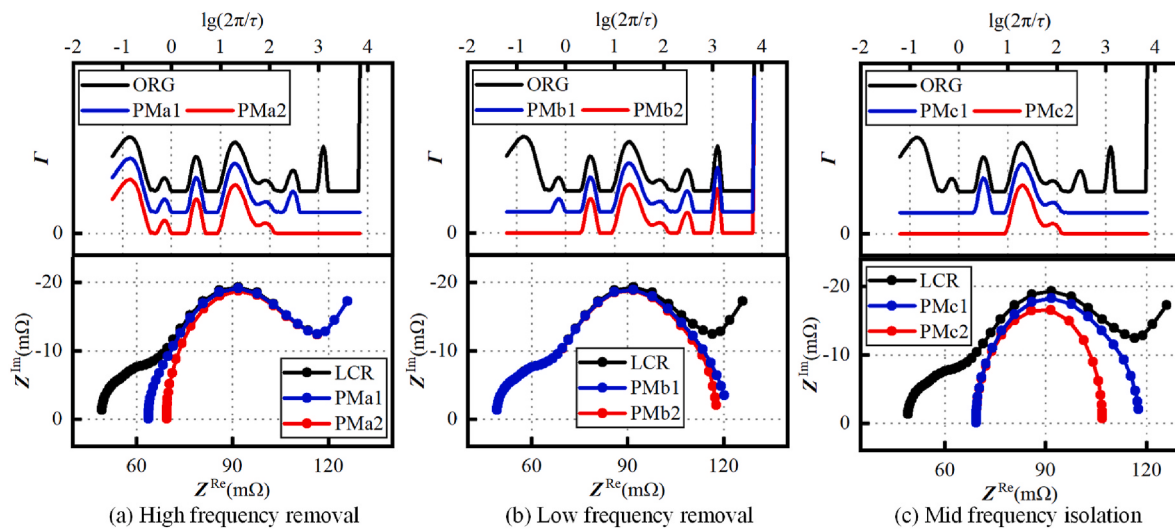


Fig. 7. EIS data manipulation examples.

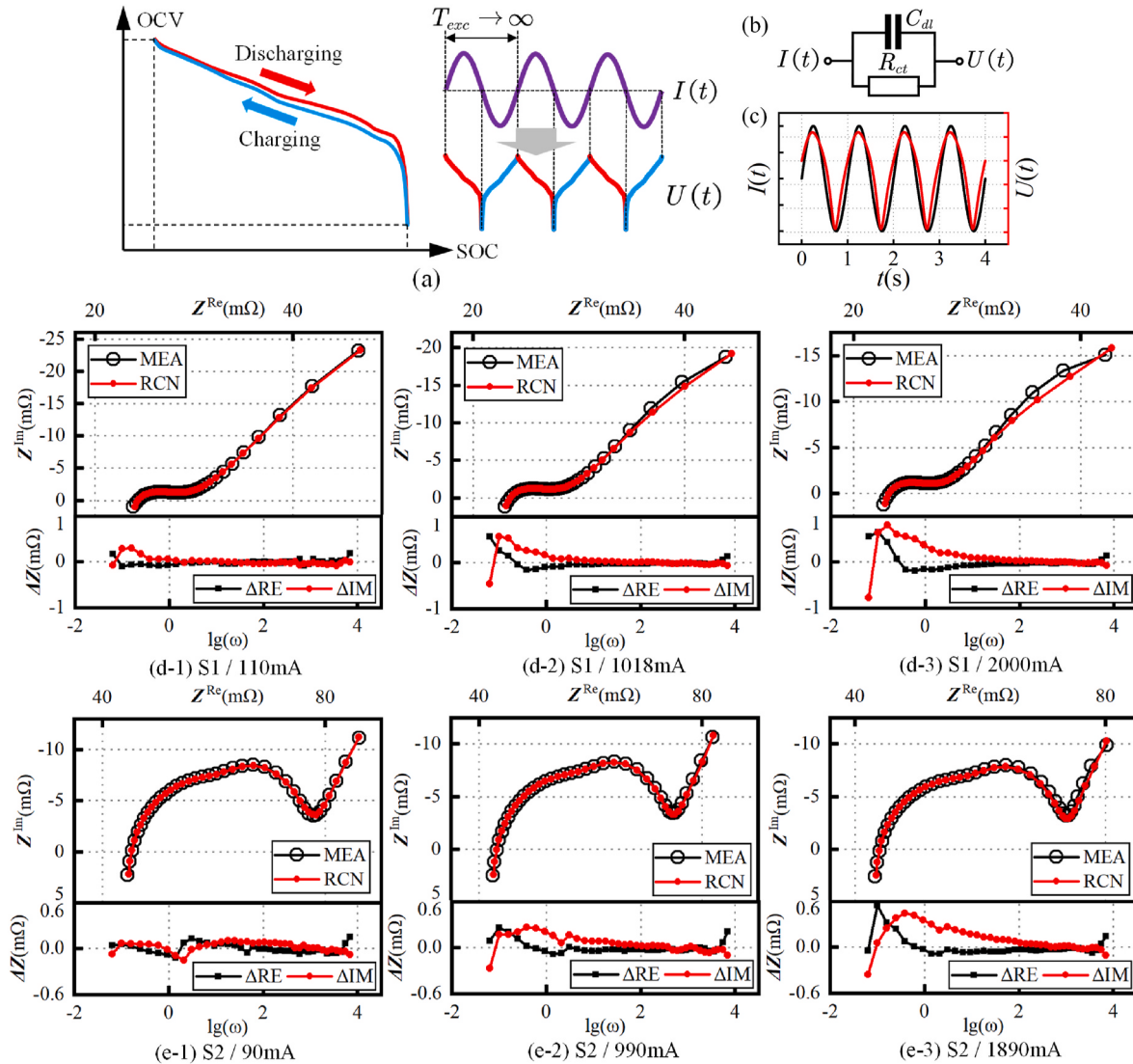


Fig. 8. (a) Speculation of response with OCV, (b–c) nonlinearity introduced by the interfacial reaction, (d–e) diagnosis of low-frequency EIS.

infinite and the relation $IT_{exc}/2 = Q$ holds, where Q is the rated capacity of the battery, it is easy to speculate the waveforms of the excitation and response in the time domain as Fig. 8(a). Under the sinusoidal current excitation, the voltage response follows the pattern of OCV curve along both charge and discharge direction. The impedance corresponding to Fig. 8(a) is purely dependent on the characteristics of the electrode material, i.e., the impedance cannot be reasonably analyzed or interpreted without the knowledge of OCV. Although the stationarity is satisfied, the prerequisite of linearity is apparently compromised as the voltage waveform $U(t)$ in Fig. 8(a) is abundant in higher-order harmonics.

As for the interfacial reaction, a classical equivalent circuit as shown in Fig. 8(b) is introduced. R_{ct} is the well-known charge transfer resistance, which is implemented according to the Butler-Volmer condition, and C_{dl} is the interfacial capacitance, which is attributable to the electric double layer. The voltage response for this equivalent circuit in the time domain using feasible parameters is simulated and given in Fig. 8(c). Without Fourier transform, it can be easily judged that the sum of the second- and higher-order harmonics for the corresponding impedance is relatively high.

As depicted in Fig. 3(e–f), although the low-frequency region of the EIS tested with small current is much smoother than the high-frequency region, the SNR still remains questionable. Accurate measurement of EIS at low frequencies stands as a dilemma, requiring trade-off between data validity and nonlinearity as well as time-variance, since the boundary between the frequency and time domain blurs. If, as in this paper, multiple sets of data with different currents are obtained, surface interpolation can be used to estimate the zero-current EIS. With a large amount of data at hand, it is also possible to manually set the profile of test current for minimizing the nonlinearity and time-variance, as suggested in [54] by judging the amount of the total-harmonics-distortion (THD) during test.

The above analysis faces with the same end that the low-frequency correction of EIS without prior knowledge is basically unfeasible. DRT-based methods generally require little prior knowledge, and thus it cannot effectively compensate for the nonlinearity and time-variance regarding the mid- and low-frequency regions. Although it is impossible to quantify the impacts of the nonlinearity and time-variance, method based on DRT transform is still able to intuitively determine whether the measured EIS data are affected and the degree to which they are affected. Selecting a suitable kernel for DRT transform, as in equation (21), and then using the same kernel for inverse DRT transform of the resulting distribution function, as in equation (34) or (35), it is convenient to compare the degree to which the original EIS are affected by nonlinearity and time-variance. Fig. 8(d–e) shows the diagnostic results of the two commercial batteries S1 and S2 at 90%SOC under different currents, and visualizes the errors between the real and imaginary parts of the reconstructed EIS (RCN) and those of the original EIS (MEA) at different frequencies. As the current increases significantly, the impedance fitted by the DRT transform at lower frequencies presents larger errors, which can also be seen from the Nyquist plots. Since the DRT transform seeks to find the best distribution function that fits the kernel, the error depicted represents the mere residual that cannot be linearized according to the solving kernel, rather than all the components caused by the nonlinearity and time-variance, because of the inability to decouple the nonlinear and time-varying components without sufficient prior knowledge. Such impedance errors cannot be completely eliminated due to the measurement noise and the non-ideality of EIS test. The larger the impedance error in Fig. 8(d–e), the lower the usability of the corresponding data points.

4.5. Application of the preprocessing schemes

The usage of EIS lies in many aspects as mentioned in Chapter I. Before using the raw EIS data for these purposes, it is necessary to check their legitimacy to prevent drawing misleading conclusions. The

experimenter needs to keep in mind that the EIS could be potentially distorted, and the central factors should be properly controlled. It is indeed possible to test specially in non-stationary states, such as the nonlinear EIS or online EIS, but the complexity in such cases calls for closer study. However, if the linear time-invariant impedances in these cases are successfully recovered, the preprocessing presented here can also be applied. Whether using laboratory electrochemical workstation or on-vehicle impedance acquisition device, inductive factors can always come in the way. Therefore, it is recommended to perform the inductance correction in Section 4.1 to first rule out this part of the interference.

The core of interpreting the kinetics is decoupling and try to achieve precise fitting of the theories. In this case, high linearity and time-invariance should generally be present. DRT-based EIS validation can be carried out according to Section 4.2 and 4.4 to determine the degree of the usability, laying a reliable basis for the theoretical analysis. For the impedance satisfying the prerequisites, DRT transform can be further performed to obtain the temporal distribution of the electrochemical processes. Regarding the concerned DRT peaks, comparison under different conditions can be realized by isolation as per Section 4.3, so as to explore the properties and mechanisms of specific kinetics.

Battery state estimation is an important engineering application of EIS. The idea is to associate the deformation of EIS with states such as the SOC, SOH, and internal temperature. The anchor for these states is mostly the linear time-invariant EIS. Therefore, impedance check in Section 4.2 and 4.4 of the inductance-corrected EIS should be carried out. For EIS acquired online, not only the inductance is eliminated by the correction in Section 4.1, but also the linearization and the filtering of EIS are conducted, which brings conveniences for further work. For DRT peaks strongly correlated with the internal states, EIS data manipulation in Section 4.3 can be used to focus on the electrode behavior falling into the interested frequency range so that the accuracy of the state identification can be improved.

5. Conclusions

DRT-based preprocessing of EIS data without much prior knowledge is systematically discussed in this paper. The DRT approach is systematically analyzed from both the solving kernel and the solving method. With the rigorous mathematical derivation, implicit connection between the solving kernel and the K–K relations is revealed, paving a new path for the EIS data validation with DRT transform and its inverse. The practical applications of DRT in EIS preprocessing are also demonstrated on the basis of in-depth theoretical analysis. EIS data is vulnerable to the parasitic inductance of the testbench, and three solving kernels are adopted to correct and compensate the consequential high-frequency distortion in EIS data, so as to facilitate the analysis of the electrochemical processes for LIB. Prior to further utilization, violation of the EIS test prerequisites in the raw EIS data is checked, and the procedures for DRT-based EIS data validation are given according to the theoretical derivations. The distribution function obtained from DRT transform includes insightful leads on the electrochemical processes, enabling the flexible modification and isolation of the EIS in a process-oriented manner. By modifying the shape, adjusting the position, deleting or adding of DRT peak, the impact of a specific process contained in the EIS can be altered. The theoretical basis and procedures are given to meet the realistic needs of the EIS data manipulation. The low-frequency region of EIS could suffer from significant nonlinearity and time-variance. The DRT transform can provide an intuitive judgment on whether and how much the EIS is degraded, and realizes the diagnosis of EIS at low frequency. The EIS preprocessing schemes with DRT transform are validated with the experimental data from commercial batteries, and manifest wide feasibility and high practicality. As the impedance-based applications in battery management attracts growing attention, the ideas elaborated in this paper are expected to provide useful instructions for the reliable implementation of EIS technique in the automotive

industry.

CRediT authorship contribution statement

Bowen Yang: Conceptualization, Software, Validation, Visualization, Writing – original draft, Writing – review & editing. **Dafang Wang:** Supervision, Funding acquisition, Resources, Project administration. **Shiqin Chen:** Methodology, Validation, Data curation. **Xu Sun:** Validation, Visualization. **Beike Yu:** Data curation, Software, Visualization, Writing – review & editing.

Declaration of competing interest

The authors declare that they have no known competing financial interests or personal relationships that could have appeared to influence the work reported in this paper.

Data availability

Data will be made available on request.

Acknowledgments

This work was supported by the National Natural Science Foundation of China (No. 52177210).

References

- [1] N. Meddings, M. Heinrich, F. Overney, J.S. Lee, V. Ruiz, E. Napolitano, S. Seitz, G. Hinds, R. Raccichini, M. Gaberšček, J. Park, Application of electrochemical impedance spectroscopy to commercial Li-ion cells: a review, *J. Power Sources* 480 (2020), <https://doi.org/10.1016/j.jpowsour.2020.228742>.
- [2] A. Barai, K. Uddin, M. Dubarry, L. Somerville, A. McGordon, P. Jennings, I. Bloom, A comparison of methodologies for the non-invasive characterisation of commercial Li-ion cells, *Prog. Energy Combust. Sci.* 72 (2019), <https://doi.org/10.1016/j.pecs.2019.01.001>.
- [3] W. Choi, H.C. Shin, J.M. Kim, J.Y. Choi, W.S. Yoon, Modeling and applications of electrochemical impedance spectroscopy (Eis) for lithium-ion batteries, *J. Electrochem. Sci. Technol.* 11 (2020), <https://doi.org/10.33961/jecst.2019.00528>.
- [4] F. Ciucci, Modeling electrochemical impedance spectroscopy, *Curr. Opin. Electrochem.* 13 (2019), <https://doi.org/10.1016/j.coelec.2018.12.003>.
- [5] H. Nara, T. Yokohima, T. Osaka, Technology of electrochemical impedance spectroscopy for an energy-sustainable society, *Curr. Opin. Electrochem.* 20 (2020), <https://doi.org/10.1016/j.coelec.2020.02.026>.
- [6] K. Rumpf, M. Naumann, A. Jossen, Experimental investigation of parametric cell-to-cell variation and correlation based on 1100 commercial lithium-ion cells, *J. Energy Storage* 14 (2017), <https://doi.org/10.1016/j.est.2017.09.010>.
- [7] F.J. Günter, J.B. Habedank, D. Schreiner, T. Neuwirth, R. Gilles, G. Reinhart, Introduction to electrochemical impedance spectroscopy as a measurement method for the wetting degree of lithium-ion cells, *J. Electrochem. Soc.* 165 (2018), <https://doi.org/10.1149/2.0081814jes>.
- [8] V. Vivier, M.E. Orazem, Impedance analysis of electrochemical systems, *Chem. Rev.* 122 (2022) 11131–11168, <https://doi.org/10.1021/acs.chemrev.1c00876>.
- [9] H. Piret, P. Granjon, N. Guillet, V. Cattin, Tracking of electrochemical impedance of batteries, *J. Power Sources* 312 (2016), <https://doi.org/10.1016/j.jpowsour.2016.02.006>.
- [10] A. La Rue, P.J. Weddle, M. Ma, C. Hendricks, R.J. Kee, T.L. Vincent, State-of-Charge estimation of LiFePO₄–Li₄Ti₅O₁₂ batteries using history-dependent complex-impedance, *J. Electrochem. Soc.* 166 (2019), <https://doi.org/10.1149/2.0221916jes>.
- [11] R. Xiong, J. Tian, H. Mu, C. Wang, A systematic model-based degradation behavior recognition and health monitoring method for lithium-ion batteries, *Appl. Energy* 207 (2017), <https://doi.org/10.1016/j.apenergy.2017.05.124>.
- [12] P. Haussmann, J. Melbert, Internal cell temperature measurement and thermal modeling of lithium ion cells for automotive applications by means of electrochemical impedance spectroscopy, *SAE Int. J. Altern. Powertrains.* 6 (2017), <https://doi.org/10.4271/2017-01-1215>.
- [13] X. Wang, X. Wei, Q. Chen, J. Zhu, H. Dai, Lithium-ion battery temperature on-line estimation based on fast impedance calculation, *J. Energy Storage* 26 (2019), <https://doi.org/10.1016/j.est.2019.100952>.
- [14] A. Podias, A. Pfrang, F. Di Persio, A. Kriston, S. Bobba, F. Mathieu, M. Message, L. Boon-Brett, Sustainability assessment of second use application of automotive batteries: ageing of li-ion battery cells in automotive and grid-scale applications, in: *EVS 2017 - 30th Int. Electr. Veh. Symp. Exhib.*, 2017.
- [15] J. Li, C. Arbizzani, S. Kjelstrup, J. Xiao, Y. Yao Xia, Y. Yu, Y. Yang, I. Belharouak, T. Zawodzinski, S.T. Myung, R. Raccichini, S. Passerini, Good practice guide for papers on batteries for the *Journal of Power Sources*, *J. Power Sources* 452 (2020), <https://doi.org/10.1016/j.jpowsour.2020.227824>.
- [16] S. Ernst, T.P. Heins, N. Schlüter, U. Schröder, Capturing the current-overpotential nonlinearity of lithium-ion batteries by nonlinear electrochemical impedance spectroscopy (NLEIS) in charge and discharge direction, *Front. Energy Res.* 7 (2019), <https://doi.org/10.3389/fenrg.2019.00151>.
- [17] N. Harting, N. Wolff, U. Kreuer, Identification of lithium plating in lithium-ion batteries using nonlinear frequency response analysis (NFRA), *Electrochim. Acta* 281 (2018), <https://doi.org/10.1016/j.electacta.2018.05.139>.
- [18] M.D. Murbach, V.W. Hu, D.T. Schwartz, Nonlinear electrochemical impedance spectroscopy of lithium-ion batteries: experimental approach, analysis, and initial findings, *J. Electrochim. Soc.* 165 (2018), <https://doi.org/10.1149/2.0711811jes>.
- [19] M.D. Murbach, D.T. Schwartz, Extending newman's pseudo-two-dimensional lithium-ion battery impedance simulation approach to include the nonlinear harmonic response, *J. Electrochim. Soc.* 164 (2017), <https://doi.org/10.1149/2.0301711jes>.
- [20] F. Fasmin, R. Srinivasan, Review—nonlinear electrochemical impedance spectroscopy, *J. Electrochim. Soc.* 164 (2017), <https://doi.org/10.1149/2.0391707jes>.
- [21] D. Andre, M. Meiler, K. Steiner, C. Wimmer, T. Soczka-Guth, D.U. Sauer, Characterization of high-power lithium-ion batteries by electrochemical impedance spectroscopy. I. Experimental investigation, *J. Power Sources* 196 (2011), <https://doi.org/10.1016/j.jpowsour.2010.12.102>.
- [22] D.A. Howey, P.D. Mitcheson, V. Yusif, G.J. Offer, N.P. Brandon, Online measurement of battery impedance using motor controller excitation, *IEEE Trans. Veh. Technol.* 63 (2014), <https://doi.org/10.1109/TVT.2013.2293597>.
- [23] B. Liebhart, L. Komsyksa, C. Endisch, Passive impedance spectroscopy for monitoring lithium-ion battery cells during vehicle operation, *J. Power Sources* 449 (2020), <https://doi.org/10.1016/j.jpowsour.2019.227297>.
- [24] B. Yang, D. Wang, B. Zhang, S. Chen, X. Sun, T. Wang, Aging diagnosis-oriented three-scale impedance model of lithium-ion battery inspired by and reflecting morphological evolution, *J. Energy Storage* 59 (2023), 106357, <https://doi.org/10.1016/j.est.2022.106357>.
- [25] A. Bartlett, J. Marcicki, S. Onori, G. Rizzoni, X.G. Yang, T. Miller, Electrochemical model-based state of charge and capacity estimation for a composite electrode lithium-ion battery, *IEEE Trans. Trans. Control Syst. Technol.* 24 (2016), <https://doi.org/10.1109/TCST.2015.2446947>.
- [26] N. Lotfi, J. Li, R.G. Landers, J. Park, Li-Ion battery state of health estimation based on an improved single particle model, *Proc. Am. Control Conf.* (2017), <https://doi.org/10.23919/ACC.2017.7962935>.
- [27] Z. Ma, Z. Wang, R. Xiong, J. Jiang, A mechanism identification model based state-of-health diagnosis of lithium-ion batteries for energy storage applications, *J. Clean. Prod.* 193 (2018), <https://doi.org/10.1016/j.jclepro.2018.05.074>.
- [28] J. Bi, T. Zhang, H. Yu, Y. Kang, State-of-health estimation of lithium-ion battery packs in electric vehicles based on genetic resampling particle filter, *Appl. Energy* 182 (2016), <https://doi.org/10.1016/j.apenergy.2016.08.138>.
- [29] Z. Deng, L. Yang, Y. Cai, H. Deng, L. Sun, Online Available Capacity Prediction and State of Charge Estimation Based on Advanced Data-Driven Algorithms for Lithium Iron Phosphate Battery, *Energy*, 2016, <https://doi.org/10.1016/j.energy.2016.06.130>.
- [30] H. Schichlein, A.C. Müller, M. Voigts, A. Krügel, E. Ivers-Tiffée, Deconvolution of electrochemical impedance spectra for the identification of electrode reaction mechanisms in solid oxide fuel cells, *J. Appl. Electrochem.* (2002), <https://doi.org/10.1023/A:1020599525160>.
- [31] Yang Lu, Chen-Zi Zhao, Jia-Qi Huang, Qiang Zhang, The timescale identification decoupling complicated kinetic processes in lithium batteries, *Joule* (2022), <https://doi.org/10.1016/j.joule.2022.05.005>.
- [32] M. Gaberšček, J. Moskon, B. Erjavec, R. Dominko, J. Jamnik, The importance of interphase contacts in Li ion electrodes: the meaning of the high-frequency impedance arc, *Electrochim. Solid State Lett.* (2008), <https://doi.org/10.1149/1.2964220>.
- [33] J. Illig, M. Ender, T. Chrobak, J.P. Schmidt, D. Klots, E. Ivers-Tiffée, Separation of charge transfer and contact resistance in LiFePO₄-cathodes by impedance modeling, *J. Electrochim. Soc.* (2012), <https://doi.org/10.1149/2.030207jes>.
- [34] H.M. Nussenzveig, *Chaper1 Causality and Dispersion Relations, Mathematics in Science and Engineering*, vol. 95, Academic Press, New York, 1972.
- [35] E. Schatzl, D.I. Stroe, K. Norregaard, L.S. Ingvarsson, A. Christensen, Incremental capacity analysis applied on electric vehicles for battery state-of-health estimation, *IEEE Trans. Ind. Appl.* (2021), <https://doi.org/10.1109/TIA.2021.3052454>.
- [36] Bowen Yang, Dafang Wang, Xu Sun, Shiqin Chen, Beike Yu, Electrochemical modeling in a building blocks' way, *Chem. Eng. J.* (2023), <https://doi.org/10.1016/j.cej.2022.140419>.
- [37] A. Barai, K. Uddin, W.D. Widanage, A. McGordon, P. Jennings, A study of the influence of measurement timescale on internal resistance characterisation methodologies for lithium-ion cells, *Sci. Rep.* (2018), <https://doi.org/10.1038/s41598-017-18424-5>.
- [38] B. Hirschorn, B. Tribollet, M.E. Orazem, On selection of the perturbation amplitude required to avoid nonlinear effects in impedance measurements, *Isr. J. Chem.* (2008), <https://doi.org/10.1560/ijc.48.3-4.133>.
- [39] T.F. Landinger, G. Schwarzberger, A. Jossen, A novel method for high frequency battery impedance measurements, in: 2019 IEEE Int. Symp. Electromagn. Compat. Signal Power Integrity, EMC+SIPI 2019, 2019, <https://doi.org/10.1109/ISEMC.2019.8825315>.
- [40] Manuel Kasper, Arnd Leike, Thielmann Johannes, Christian Winkler, Nawfal Al-Zubaidi R-Smith, Ferry Kienberger, Electrochemical impedance spectroscopy error

- analysis and round robin on dummy cells and lithium-ion-batteries, *J. Power Sources* (2022), <https://doi.org/10.1016/j.jpowsour.2022.231407>.
- [41] X. Li, M. Ahmadi, L. Collins, S.V. Kalinin, Deconvolving distribution of relaxation times, resistances and inductance from electrochemical impedance spectroscopy via statistical model selection: exploiting structural-sparsity regularization and data-driven parameter tuning, *Electrochim. Acta* (2019), <https://doi.org/10.1016/j.electacta.2019.05.010>.
- [42] B.A. Boukamp, Fourier transform distribution function of relaxation times; application and limitations, *Electrochim. Acta* (2015), <https://doi.org/10.1016/j.electacta.2014.12.059>.
- [43] E. Tuncer, S.M. Gubanski, On dielectric data analysis. Using the Monte Carlo method to obtain relaxation time distribution and comparing non-linear spectral function fits, *IEEE Trans. Dielectr. Electr. Insul.* 8 (3) (2001) 310–320, <https://doi.org/10.1109/94.933337>.
- [44] S. Hershkovitz, S. Baltianski, Y. Tsur, Harnessing Evolutionary Programming for Impedance Spectroscopy Analysis: A Case Study of Mixed Ionic-Electronic Conductors, *Solid State Ionics*, 2011, <https://doi.org/10.1016/j.ssi.2010.10.004>.
- [45] M. Saccoccio, T.H. Wan, C. Chen, F. Ciucci, Optimal regularization in distribution of relaxation times applied to electrochemical impedance spectroscopy: ridge and Lasso regression methods - a theoretical and experimental Study, *Electrochim. Acta* (2014), <https://doi.org/10.1016/j.electacta.2014.09.058>.
- [46] S. Dierickx, A. Weber, E. Ivers-Tiffée, How the distribution of relaxation times enhances complex equivalent circuit models for fuel cells, *Electrochim. Acta* (2020), <https://doi.org/10.1016/j.electacta.2020.136764>.
- [47] J. Wang, Q.A. Huang, W. Li, J. Wang, Y. Bai, Y. Zhao, X. Li, J. Zhang, Insight into the origin of pseudo peaks decoded by the distribution of relaxation times/differential capacity method for electrochemical impedance spectroscopy, *J. Electroanal. Chem.* (2022), <https://doi.org/10.1016/j.jelechem.2022.116176>.
- [48] M.B. Effat, F. Ciucci, Bayesian and hierarchical bayesian based regularization for deconvolving the distribution of relaxation times from electrochemical impedance spectroscopy data, *Electrochim. Acta* (2017), <https://doi.org/10.1016/j.electacta.2017.07.050>.
- [49] F. Ciucci, C. Chen, Analysis of electrochemical impedance spectroscopy data using the distribution of relaxation times: a Bayesian and hierarchical Bayesian approach, *Electrochim. Acta* (2015), <https://doi.org/10.1016/j.electacta.2015.03.123>.
- [50] H.A. Kramers, *La diffusion de la lumière par les atomes*, Atti Cong. Intern. Fis. (1927).
- [51] R. de L. Kronig, On the theory of dispersion of X-rays, *J. Opt. Soc. Am.* (1926), <https://doi.org/10.1364/josa.12.000547>.
- [52] J.M. Carcione, F. Cavallini, J. Ba, W. Cheng, A.N. Qadrouh, On the Kramers-Kronig relations, *Rheol. Acta* (2019), <https://doi.org/10.1007/s00397-018-1119-3>.
- [53] M. Schönleber, D. Klotz, E. Ivers-Tiffée, A method for improving the robustness of linear kramers-kronig validity tests, *Electrochim. Acta* (2014), <https://doi.org/10.1016/j.electacta.2014.01.034>.
- [54] J.J. Giner-Sanz, E.M. Ortega, V. Pérez-Herranz, Total harmonic distortion based method for linearity assessment in electrochemical systems in the context of EIS, *Electrochim. Acta* (2015), <https://doi.org/10.1016/j.electacta.2015.10.152>.